Optimization of the hygrothermal performance of novel metal-organic framework (MOF) based humidity pump: A CFD approach

Kan Zu, Menghao Qin*

Department of Civil Engineering, Technical University of Denmark, Lyngby, Denmark

*Corresponding email: menqin@byg.dtu.dk

Abstract: Solid desiccant humidity pump is an emerging device that enables moisture transport through the inverse gradient of vapor concentration, featuring refrigerant-free, no moveable parts and compact structure. However, traditional materials (e.g. silica gel and zeolite) have made this device less competent due to the poor sorption performance and strict regeneration conditions. In this respect, metal-organic frameworks, representing the cutting edge of the available porous materials, are expected to upgrade the performance of this device. In this study, the optimization of a novel MOF-based humidity pump (MOF-HP) was carried out. We used the CFD method to analyze the hygrothermal performance of a MOF-HP. The model built up the relationship among humid air, desiccant, and heat sink and then coupled the subdomains of the fluid flow, heat transfer, and specie transport. The model of MOF-HP under different operation conditions was validated by experimental tests. Based on the measured results, the discrepancies were maintained under 15%. A parametric optimization was subsequently carried out to enhance the hygrothermal performance of MOF-HP. This dimensional analysis provides some guidelines for MOF-HP design with the most suitable geometry. The optimized configuration is estimated to have a 1.59 times improvement in moisture removal capacity over the original design.

Keywords: MOF, humidity pump, moisture transport, CFD, optimization

1. Introduction

The world's demand for comfort cooling is proliferating. Space cooling will become the single largest user of electricity in buildings, accounting for 16% of the global electricity demand by 2050 [1]. The majority of this growth will come from emerging economies with hot and humid climates. The regulation of the latent load remains a critical problem for energy-efficient cooling. Harsh hygrothermal conditions affect the performance and lifespan of sensitive products (e.g., cultural relics, high-precision instruments) and are far from the desired thermal comfort of human beings [2, 3]. In this regard, smart thermal and moisture control technologies will significantly influence the environmental quality of indoor living spaces as well as some special places (e.g., drug storage, museums, and archives, etc.) [4]. The traditional vapor-compression refrigeration remains the most popular dehumidification method for indoor hygrothermal control. It condenses the moisture out of the air by cooling the air below the dew point and then reheating the process air to the desired supply air, which leads to increased energy consumption for the whole system [5]. In the past decades, desiccant-coated dehumidification systems have gained much more interest due to the high energy-saving potential and flexible system structures [6]. Here the desiccant adsorbs the water vapor from the air while releasing the adsorption heat and could then be regenerated by low-grade energy such as solar energy and waste heat. By taking advantage of the temperature gradient among the heat exchanger, desiccant coating, and the air, the temperature and the humidity level can be reasonably regulated for different occasions, for example, the personal comfort system (PCS) [7]. To address the drawbacks of traditional heating, ventilation, and air conditioning (HVAC) systems, the development of some novel PCS has gained much more interest. It is reported that PSC can not only satisfy more percentage of occupants than traditional air conditioning systems but also save energy consumption by 4%-60% [7]. Therefore, according to the definition of PCS, it is feasible to fabricate a compact and high-performance device to achieve the

hygrothermal regulation of a localized space by integrating the cooling unit with solid desiccant technology.

To date, among all the working principles to achieve the efficient moisture control for a solid desiccant system [8-11], a near-isothermal dehumidification process can directly turn the process air (e.g., outdoor air or return air) into the desired supply air condition [12, 13]. In this regard, the construction of SDHP depends on the design of the system framework and the selection of desiccants. Many have reported the applications of the combination of desiccant and cooling units (e.g., desiccant wheel, desiccant-coated heat exchanger). However, these devices still have some challenges to control the temperature and humidity level for a localized space: 1) the bulky size of the integrated system using traditional materials; 2) complex and long refrigerant passage; 3) low operation efficiency. Many studies have reported the corresponding applications in experiments and simulations, and many possessed large-scale systems. Wang et al. [14-17] have developed some desiccant-coated heat pump systems to control the sensible and latent loads of indoor air with good operation performance, and the mathematical models based on the lumped methods or average bulk methods have been developed. Vivekh et al. [18] utilized the CFD approaches to investigate the silica gel, and polymer employed heat exchanger. The model combined the fluid flow with the temperature and moisture distributions for all the calculated domains. The parametric study provides insight into the enhancement of moisture removal on the fin-tube heat exchanger. Recently, Fathieh et al. [19, 20] have prepared some small-scale energy exchangers to investigate its possible application in the energy wheel, which was constructed by inserting desiccant-coated aluminum sheets between two plastic frames. The results indicate the increase of latent effectiveness and the effect of flow rate and temperature on the regeneration process. Li et al. [21] have designed a silica gel-based humidity pump for localized humidity control. This

device has shown a flexible structure to the moisture regulation with low cost-effectiveness, and the humidity transfer rate can approach a comparable value. On the other hand, the commonly used desiccants such as zeolite and silica gel possess a relatively low adsorption capacity on the working relative pressure range and strict regeneration condition, thus promoting the modification of conventional materials and the exploitation of novel materials.

In recent years, metal-organic framework (MOF) emerged as a novel desiccant material gain much more interest [6, 22-24]. It is known that MOFs consist of metal clusters and organic linkers to form a homogeneous structure in nature. Many MOFs have S-shaped isotherms, stable cycling performance, and mild regeneration conditions [25, 26]. However, according to our previous work [6], many MOF materials are still limited by either operation performance or safety risk. A green and cost-effective MOF material should be the top priority. Recently, MIL-160(Al), a hydrophilic carboxylate MOF, has been proposed [27, 28], and the tests of gravimetric water loading lifts have shown that the loading lift of MIL-160(Al) is 2.5 times higher than that of silica gel. Permyakova et al. [28] optimized the synthetic route and investigated its energy storage on the open-system prototype. Schlüsener et al. [29] adopted different ratios of the organic linkers (mixed-linker) to tune the hydrophilicity of MIL-160(Al), and higher COP values have been reported.

In our previous work, a novel MOF-based humidity pump (MOF-HP) was fabricated to achieve energy-efficient localized moisture control [30]. Though some have reported a similar device [21, 30], the corresponding optimization based on the real multi-physical field (e.g., fluid flow, heat, and mass transfer) has little been reported, not even CFD approach [18]. In this paper, the optimization of the hygrothermal transfer performance of MOF-HP will be carried out by using the CFD approach. Theoretically, the heat transfer enhancement can improve the mass

transport and thus the whole performance. For the design of MOF-HP, the factors such as the adsorption heat and mass transfer rate from the desiccant layer and the overall thermal resistance are directly related to the operation performance. A creative design able to enhance mass transfer and reduce the thermal resistance of the device is the primary object of this work. Here a three-dimensional physical model of MOF-HP has been developed considering the fluid flow domain, mass transfer domain, and heat transfer domain. MIL-160(Al) is selected and prepared as the desiccant layer. Moreover, the subsequent optimization studies are conducted to investigate the effect of configuration design on the computational domains. The validated experiments and detailed sensitivity analysis are provided, and the corresponding results are compared to an elemental heat sink without the desiccant layer.

2. Materials and methods

2.1 Material

The preparation of MIL-160(Al) was based on the reported ref. [31]. The solvothermal synthesis route can help synthesize MIL-160(Al) via the chemical reaction of Aluminum acetate and FDCA (2,5-furandicarboxylicacid). 1:1 of Aluminum acetate and FDCA were mixed in a container filled with deionized water and then stirred for 24h under the reflux condition. The reaction product was purified by deionized water and ethanol at room temperature for 3h and finally dried in a vacuum oven (100℃) to produce the white solid MIL-160(Al).

2.2 System analysis

This work aims to investigate the effect of geometrical factors and flow field on the heat and mass transfer to maximize the efficiency of MOF-HP on moisture management. In this case, a 3D model (Fig.1) integrating heat transfer, mass transport, and flow domains was developed to

study the geometrical optimization of the MOF-HP. The coating treatment on the fins of the heat sink was adopted in the MOF-HP by referring to other reported configurations [15, 32, 33]. It is noted that the desiccant coating is only considered at the surface of fins in the experiments. The geometry of MOF-HP is shown with details in Table 1.

Table 1 The geometry of MOF-HP.

Parameters	Values
Length of the flow passage, cm	20
Width of the flow passage, cm	6
Height of the flow passage, cm	5
Length of the heat sink (L_x), cm	10
Width of a single channel in the heat sink (W_y), cm	0.495
Height of heat sink (H_z), cm	5
Fin thickness (W_f), cm	0.05
Fin pitch (W_{gap}), cm	0.445
No. of fins (NUM)	11

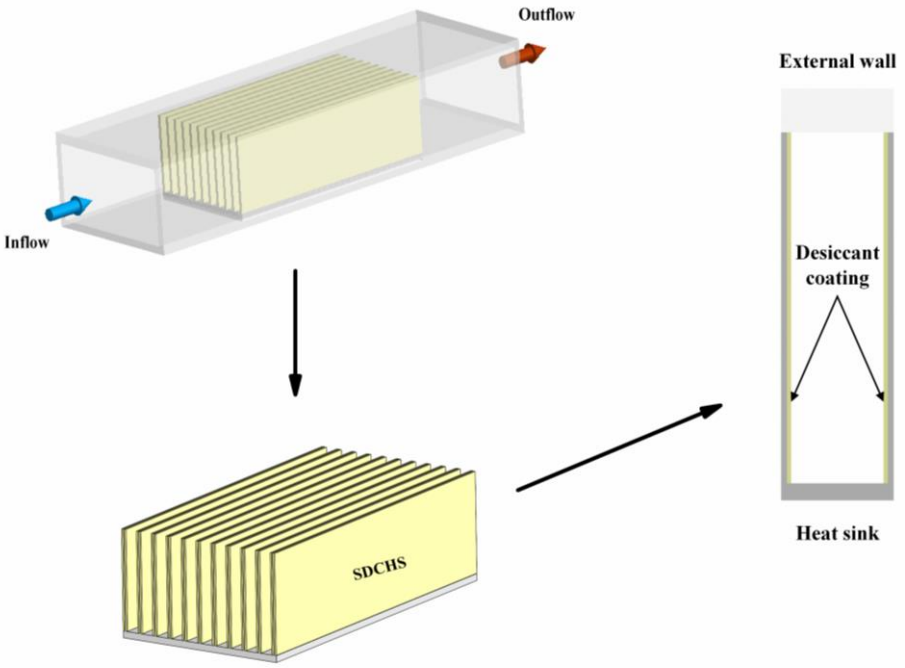

Fig.1. The schematic of MOF-HP.

The fluid in the flow field is humid air, and the solid part of the supporting framework (heat sink) is aluminum alloy. The heat sink was manufactured with specifications shown in Table 1. MOF desiccant- MIL-160(Al) was coated on the surface of fins on the heat sink after the dip-coating process (net weight of coatings: 24.3g). The initial and final mass of the heat sink was measured, and then the thickness was deduced based on the density of desiccant and available coating surface area. The obtained thickness of MOF coatings was compared with the directly measured value using vernier calipers with an accuracy of 0.01mm.

The experiments were designed to measure the cycling performance (i.e., dehumidification and regeneration) of MOF-HP. An air preheater and an ultrasonic humidifier were utilized to control the inlet air states, such as the temperature and humidity. During the dehumidification process, the process air was transmitted by fans to achieve heat and mass transport in the MOF-HP. The desiccant coating removes the extra moisture load, and the heat sink transfers the sensible load. The heat flux from the bottom side of the heat sink can regulate the supply air

temperature within a desirable range. When the desiccant coatings approach the saturated state, switching the heat flux from the bottom side of the heat sink can turn the dehumidification mode into regeneration mode. The inlet air with the same conditions passed through the MOF-HP to bring the released moisture away, and this hot and exhaust air was then rejected outdoors. Two digital hygro sensors (SEK-SHTC3-Sensors, Sensirion) were prepared at the inlet and outlet of this device to measure the temperature and relative humidity, which have a 0.5s interval time with an accuracy of ±0.2 °C and ±2% RH. The airflow rate was controlled by a variable frequency fan and measured by an anemograph (Testo 410-1).

3. Mathematical model

Considering that the flow state is in laminar flow (*Re* number is around 250), Fig.2(a) shows the modeling framework of the MOF-HP for the computational study, and it can be seen as the combination of many uniform unit channels. The single unit channel is used as the computational domain with the size of $L_x*W_y*H_z$. The geometry in detail is shown in Fig.2(b). According to the symmetric geometry of the unit channel, it is reasonable to simplify the flow domain by the symmetry principle [34]. The unit channel with a height of H_z and width of W_y has a half aluminum fin with a thickness of W_f and height of H_f, heat sink base with a thickness of *Hs*, and desiccant coating with a thickness of *Wd*. Multiphysics fields have been simulated based on the 3D computational model, and the operation principles of the MOF-HP are shown in Fig.2(c), including dehumidification and regeneration processes. There are some assumptions on the following mathematical model:

- The mass distribution of desiccants on the fins is even (relative mass difference of each fin is less than ±5%);
- Local mass equilibrium is assumed on the interface between desiccant and air domain;
- The fluid in the air domain is assumed to be incompressible and steady;

- Thermophysical properties of the desiccant domain (i.e., density, heat capacity, and thermal conductivity) are regarded as the constants in the operating conditions;
- In the desiccant domain ($\overrightarrow{u_a} = 0$), the desiccant coatings are considered as in solid state when coated on the surface of fins;
- The radiation effect is not considered in this model, and the walls of this device are insulated to the ambient conditions.

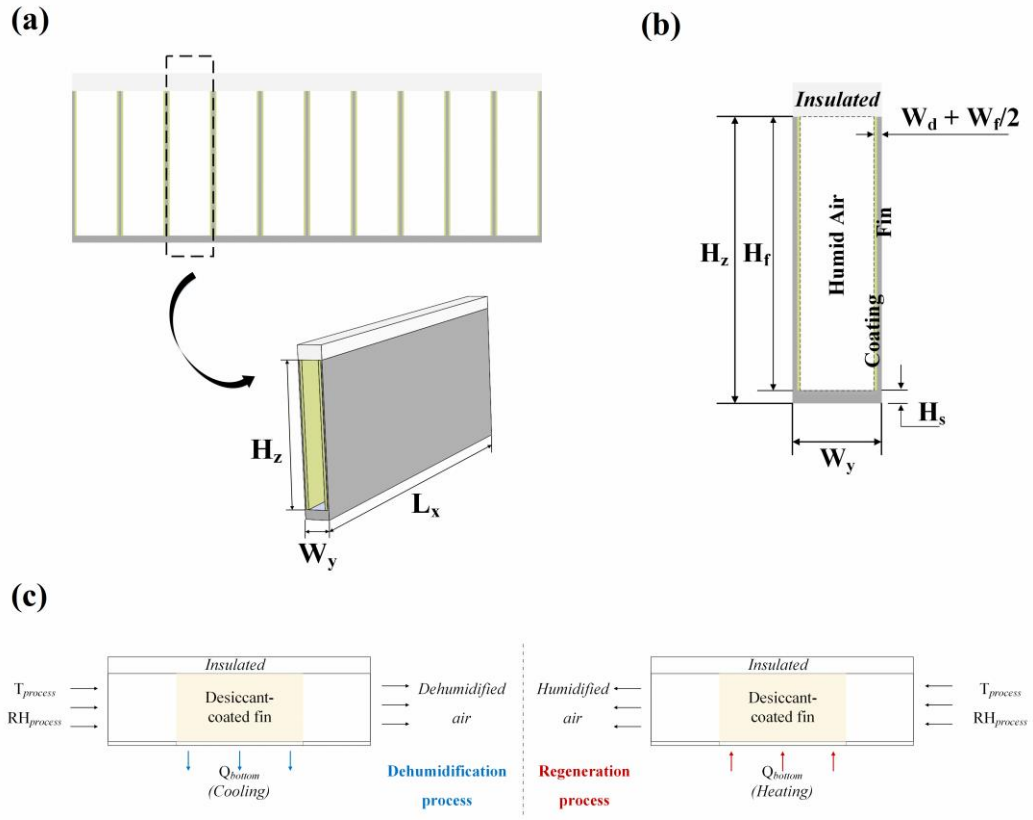

Fig.2. The schematic of the computational domain. a) A unit channel; b) Geometry; c) Operation principles.

3.1 Governing equations

Based on the assumptions, the governing equations of different computational domains with the corresponding initial and boundary conditions are evaluated simultaneously. Eqs (1)-(3) describe energy conservation and species conservation in the desiccant domain. Eqs. (4)-(8)

indicate the continuity, momentum and energy conservation, and species equilibrium from the air domain. As for the heat sink domain, energy conservation is employed as shown in Eqs. (9)-(10).

Desiccant domain:

$$\frac{\partial c_d}{\partial t} = -\nabla \cdot \vec{\boldsymbol{J}} \tag{1}$$

$$(\rho C_p)_d \frac{\partial T_d}{\partial t} = -\nabla \cdot \overrightarrow{\boldsymbol{q_d}} \tag{2}$$

$$\vec{\boldsymbol{J}} = -D_d \nabla c_d,\ \overrightarrow{\boldsymbol{q_d}} = -\lambda_d \nabla T_d \tag{3}$$

Air domain:

$$\nabla \cdot (\rho \overrightarrow{\boldsymbol{u_a}}) = 0 \tag{4}$$

$$\rho_a \frac{\partial \overrightarrow{\boldsymbol{u_a}}}{\partial t} + \rho_a (\overrightarrow{\boldsymbol{u_a}} \cdot \nabla) \overrightarrow{\boldsymbol{u_a}} = \nabla \cdot (-p\vec{\boldsymbol{I}} + \overrightarrow{\boldsymbol{K}}) \tag{5}$$

$$\frac{\partial c_v}{\partial t} + \overrightarrow{\boldsymbol{u_a}} \cdot \nabla c_v = -\nabla \cdot \vec{\boldsymbol{g}} \tag{6}$$

$$\left(\rho c_p\right)_a \left(\frac{\partial T_a}{\partial t} + \overrightarrow{\boldsymbol{u_a}} \cdot \nabla T_a\right) = -\nabla \cdot \overrightarrow{\boldsymbol{q_a}} \tag{7}$$

$$\vec{\boldsymbol{g}} = -D_v \nabla c_v,\ \overrightarrow{\boldsymbol{q_a}} = -\lambda_a \nabla T_a \tag{8}$$

Heat sink domain:

$$(\rho C_p)_{Al} \frac{\partial T_{Al}}{\partial t} = -\nabla \cdot \overrightarrow{\boldsymbol{q_{Al}}} \tag{9}$$

$$\overrightarrow{\boldsymbol{q_{Al}}} = -\lambda_{Al} \nabla T_{Al} \tag{10}$$

Where $\vec{\boldsymbol{I}}$ represents the unit vector, and $\overrightarrow{\boldsymbol{K}}$ is given by $\overrightarrow{\boldsymbol{K}} = \mu_a(\nabla \overrightarrow{\boldsymbol{u_a}} + (\nabla \overrightarrow{\boldsymbol{u_a}})')$. In Eq. (2), the adsorption heat as an internal heat source is not integrated into the equation. Since the adsorption heat was released at the interface between the air and desiccant coatings, the adsorption heat can be simplified as a boundary condition described in Section 3.2. This approach is also applicable to mass transport at the same position [18].

3.2 Properties equations

3.2.1 Surface diffusion and vapor diffusion

The adsorbed water in the desiccant coatings conducts surface diffusion, indicating the vapor transport inside the desiccant domain. In this regard, surface diffusion has been used for the operation cycles, which is a temperature-dependent variable based on the Arrhenius equation [35].

$$D_d = D_{d,0}\exp(-\frac{\alpha}{RT_d}) \tag{11}$$

Where $D_{d,0}$ and α can be determined through the experimental results. R is the gas constant [J/(mol·K)].

Water vapor diffusion in the air can be calculated by using the following correlation [36]:

$$D_v = \frac{2.26}{p_{atm}}(\frac{T_a}{273.15})^{1.81} \tag{12}$$

3.2.2 Isotherms and adsorption heat

The evaluation of the equilibrium sorption capacity plays a vital role in solving the governing equations. The amount of the equilibrium sorption capacity can vary according to relative humidity (or vapor pressure and temperature). The representative equation of this MOF material is determined through the measurement of isotherms, which is shown in our previous work in details [37].

$$\overline{W_{eq}} = f(\varphi) = f(p_v, T) \tag{13}$$

Where W_{eq} is the equilibrium sorption capacity of the desiccant [kg/kg]. φ is the relative humidity [%], and p_v is the vapor pressure [Pa]. According to the Clausius-Clapeyron relation and the measured isotherms ($p_v - T - W$ diagram), the adsorption heat can be calculated as [31]:

$$\Delta H_{ads} = -R\frac{\partial \ln p_v}{\partial(\frac{1}{T})} \tag{14}$$

The calculated ΔH_{ads} maintains 52kJ/mol when the water uptake of the desiccant drops between 10% and 90% of the equilibrium sorption capacity. In this paper, the adsorption heat was set as 52kJ/mol.

3.2.3 Kinetics

By using the linear driving force (LDF) theory [38], the kinetics of desiccant can be evaluated as:

$$\frac{dW}{dt} = k(\overline{W_{eq}} - \bar{W}) \tag{15}$$

Where $\bar{W}$ represents the real-time mass ad/desorbed in the desiccant coating [kg/kg]. k is the ad/desorption rate [1/s], which can be determined through gravimetric experiments [37]. It is an overall representation of the mass transfer during the ad/desorption process of the desiccant [18, 39].

3.2.4 Moisture flux and heat flux

In each unit channel of MOF-HP, the moisture and heat transport between the air and desiccant coating can be treated as moisture (q_m) and heat flux (q_h) at the interface, which can be shown as follows:

$$q_m = k \cdot q_{m,S} \tag{16}$$

$$q_h = q_m \cdot \Delta H_{ads} \tag{17}$$

Where $q_{m,S}$ represents the surface concentration of the water vapor [mol/m^2]. This can be calculated as $q_{m,S} = W_d * (\frac{\rho_d \overline{W_{eq}}}{M_w} - c_d)$, where M_w is the molecular weight of water [kg/mol], W_d is the thickness of the coating [m].

3.3 Initial and boundary conditions

1) Initial conditions

The initial conditions are given as following equations, employed for air, desiccant, and heat sink domain, respectively.

Desiccant domain ($t = 0$):

$$T_d = T_{ini} \tag{18}$$

$$c_d = c_{d,ini} = \frac{\rho_d f(RH_{ini})}{M_w} \tag{19}$$

Air domain ($t = 0$):

$$T_a = T_{ini}, \overrightarrow{\boldsymbol{u_a}} = 0 \tag{20}$$

$$\varphi_a = \varphi_{ini} \tag{21}$$

The initial vapor concentration can be calculated based on the equation of state:

$$c_v = c_{v,ini} = \frac{p_v}{RT_{ini}} = \frac{RH_{ini} * p_{sat}}{RT_{ini}} \tag{22}$$

$$p_{sat} = 288.68 \cdot \left(1.098 + \frac{T}{100}\right)^{8.02} \tag{23}$$

Heat sink domain ($t = 0$):

$$T_{Al} = T_{ini} \tag{24}$$

2) Boundary conditions

The boundary conditions of this unit channel can be listed as below:

Inlet

$$T_a = T_{in}, RH_a = RH_{in}, \overrightarrow{\boldsymbol{u_a}} = \overrightarrow{\boldsymbol{u_{in}}} \text{ at } x = 0 \tag{25}$$

Outlet

$$-\vec{\boldsymbol{n}} \cdot \vec{\boldsymbol{g}} = 0, -\vec{\boldsymbol{n}} \cdot \overrightarrow{\boldsymbol{q_a}} = 0 \text{ at } x = L \tag{26}$$

Where $\vec{\boldsymbol{n}}$ represents the normal vector of the outlet. $\vec{\boldsymbol{g}}$ and $\overrightarrow{\boldsymbol{q_a}}$ indicate the moisture and heat flux at the outlet.

Desiccant-air interface

$$\overrightarrow{\boldsymbol{u_a}} = 0, T_a = T_d \tag{27}$$

$$-\vec{\boldsymbol{n}} \cdot \vec{\boldsymbol{J}} = q_m, -\vec{\boldsymbol{n}} \cdot \overrightarrow{\boldsymbol{q_d}} = q_h \tag{28}$$

Bottom wall

$$Q_{bottom} = -\vec{\boldsymbol{n}} \cdot \overrightarrow{\boldsymbol{q_d}} = -\lambda_{Al} \nabla T_{Al}|_n \tag{29}$$

Symmetric surfaces and insulated walls

$$-\vec{\boldsymbol{n}} \cdot \overrightarrow{\boldsymbol{q_{sys,wall}}} = 0 \tag{30}$$

Fluid flow, heat, and mass transfer domains were solved simultaneously within the unit channel of MOF-HP. The inlet air states were specified in Table 2. No-slip is assumed at the interface between fluid and solid domains. The external wall of this MOF-HP is insulated from the ambient conditions. At the surface of $y = 0$ and W_y, it is considered to be symmetric. The equivalent heat flux (Q_{bottom}) is assumed to vary in a periodic square wave function, applied at the bottom of the unit channel. The heat will be transferred through the solid domains-heat sink and then desiccant- by conduction and to the air domain- humid air, while the adsorbed or released water vapor will flow between air and desiccant coating.

Table 2 Operation conditions of MOF-HP.

Parameters	Values
Inlet air temperature	21°C
Inlet air relative humidity	65%
Dew point temperature	14.2°C

3.4 Indexes

In order to evaluate the operating performance of MOF-HP, some indexes herein can be concluded:

1) Dehumidification coefficient of performance (DCOP) and dehumidification rate (D_r)

$$\Omega_m = \int_{t_s}^{t_e} \dot{m}_a(h_{in} - h_{out})\, dt \tag{31}$$

$$\mathrm{DCOP} = \frac{\Omega_m}{\int_{t_s}^{t_e} Q_{bottom} A\, dt} \tag{32}$$

Where $\dot{m}_a$ indicates the air flow rate [kg/s]. h_{in} and h_{out} represent the enthalpy of per unit air mass at the inlet and outlet [J/kg], respectively. t_s and t_e are the beginning and end time of each dehumidification process [s].

$$\mathrm{D}_r = \frac{\int_{t_s}^{t_e} \dot{m}_a(d_{in} - d_{out})\, dt}{t_e - t_s} \tag{33}$$

$$\overline{\mathrm{D}_r} = \frac{\int_{t_s}^{t_e} \dot{m}_a(d_{in} - d_{out})\, dt}{(t_e - t_s) * NUM} \tag{34}$$

Here d_{in} and d_{out} represent humidity ratio of inlet and outlet air during the dehumidification process [g/kg]. $\overline{\mathrm{D}_r}$ indicates the dehumidification rate of a single unit channel of MOF-HP.

2) Average heat transfer and thermal resistance [34]

Reynolds number

$$Re = \frac{\rho_a u_{in} \bar{H}}{\mu_a} \tag{35}$$

Average heat transfer coefficient

$$h_{m,avg} = \left| \frac{Q_{bottom}}{\overline{T_{bottom}} - T_{process}} \right| \tag{36}$$

Average Nusselt number

$$Nu_{m,avg} = \frac{h_{m,x} \bar{H}}{\lambda_a} \tag{37}$$

Average thermal resistance

$$R_{t,avg} = \left| \frac{T_{bottom,max} - T_{process}}{Q_{bottom} A} \right| \tag{38}$$

Where $\overline{H}$ is the characteristic size of the unit channel [m], which can be calculated by $\overline{H} = 2W_{gap}H_z/(H_z + W_{gap})$. $\overline{T_{bottom}}$ and $T_{bottom,max}$ are the average temperature and maximum temperature of the bottom surface [K], respectively.

3) Heat transfer effectiveness and sensitivity coefficient

In order to evaluate the effect of heat transfer on the dehumidification performance, a subscript character, *base*, has been used to evaluate the performance of MOF-HP, which refers to the one without the desiccant coating. Average heat transfer effectiveness reflects the change in the average heat transfer coefficient of MOF-HP and the reference one.

$$\eta_1 = \frac{h_{m,avg}}{h_{m,base,avg}} \tag{39}$$

The sensitivity coefficient is defined to describe the relationship between the latent load level and the whole air enthalpy change with and without desiccant coating. It can be written as follows:

$$\eta_2 = \frac{\overline{\mathrm{D}_r}/\overline{\mathrm{D}_{r,base}}}{\Omega_m/\Omega_{m,base}} \tag{40}$$

3.5 Simulation methodology

The governing equations (Eqs. (1)-(10)) were numerically solved by using finite element analysis in COMSOL Multiphysics v5.5 software. Fig. 2(b) shows that the multiphysics fields, including fluid flow, heat transfer, and moisture transport, were fully coupled and calculated simultaneously. The parameter with the largest residual error should meet the convergence condition of lower than 10^{-6}, which is based on the manual settings in the COMSOL. Grid independence study was carried out to reduce the impact of the number of grids on the numerical results while maintaining a reasonable time for the simulations. The variations of humidity ratio and temperature were calculated with the mesh accuracy increased from 641,643 elements (coarser) to 1,590,240 elements (finer). In Fig. 3, the calculated results have shown

the independent research of the mesh refinement. Consequently, the grid scheme of 641,643 elements is applied in this work.

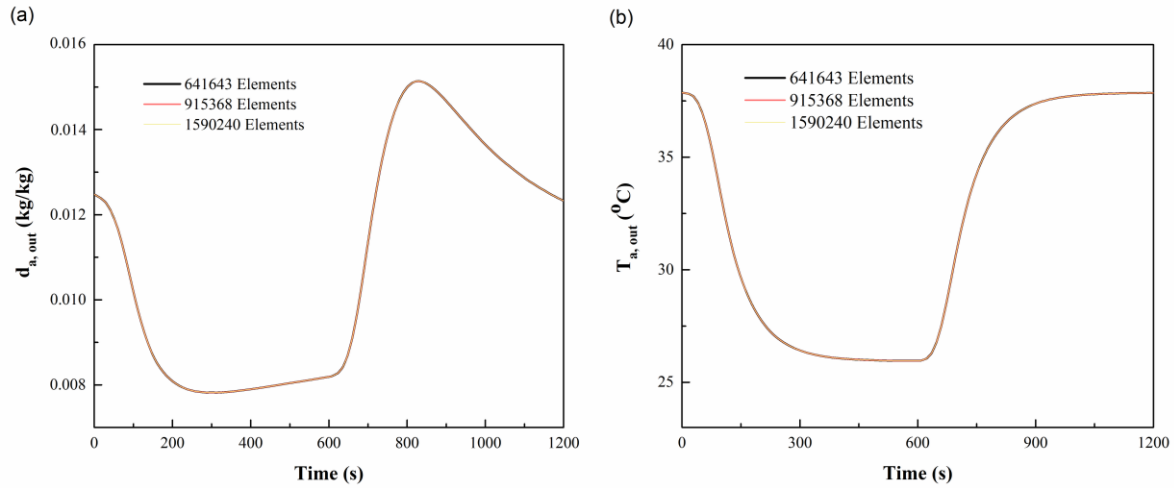

Fig.3. Grid independence study of the computational model. a) Humidity ratio; b) Temperature.

4. Validation

4.1 Surface diffusion, D_d

It is known that surface diffusion can affect the concentration gradient of the adsorbed water and thus the overall mass transfer coefficient. To the best of our knowledge, many have reported that surface diffusion is a sorption property parameter dependent on the local temperature. Consequently, the Arrhenius equation can be used to the sorption layers to evaluate the surface diffusion against the temperature variation. As shown in Eq. (11), the equation can be rearranged by $\ln(\frac{D_d}{D_{d,0}}) = -\frac{\alpha}{RT_d}$, and it is clear that there is a linear correlation between $\ln(D_d)$ and $\frac{1}{T_d}$. In Fig. 4, the Arrhenius plot shows the logarithm of surface diffusion to the inverse temperature. Thus, the fitting parameters, $D_{d,0}$ and α, can be obtained for different conditions, which are 2.14×10^{-11} m^2/s and 2.93×10^4 J/mol for *adsorption process* and 1.24×10^{-5}m^2/s and 1.16×10^4 J/mol for *desorption process*, respectively.

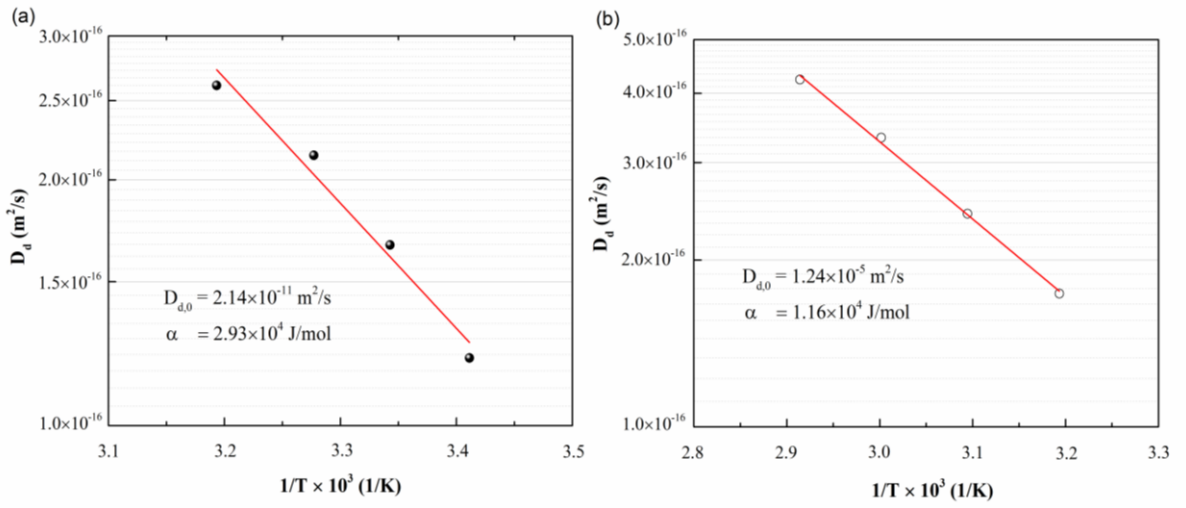

Fig.4 The correlation between temperature and mass diffusion. a) Adsorption at 65%RH; b) Desorption at 10%RH.

4.2 Validation of the model

In this section, the computational modeling is validated through the experiments obtained from the MOF-HP. The control variables used in the simulation are identical to the test conditions specified in Table 3. According to these conditions, Fig. 5 compares the transient behavior of outlet air states between the simulation and experiment for MOF-HP. It can be found that the simulated results qualitatively agree well with the experimental data. The comparison of the discrepancies between simulated and experimental results is shown in Fig. 6, and the overall discrepancy in predicting the humidity ratio and temperature is within a reasonable range of ±15%.

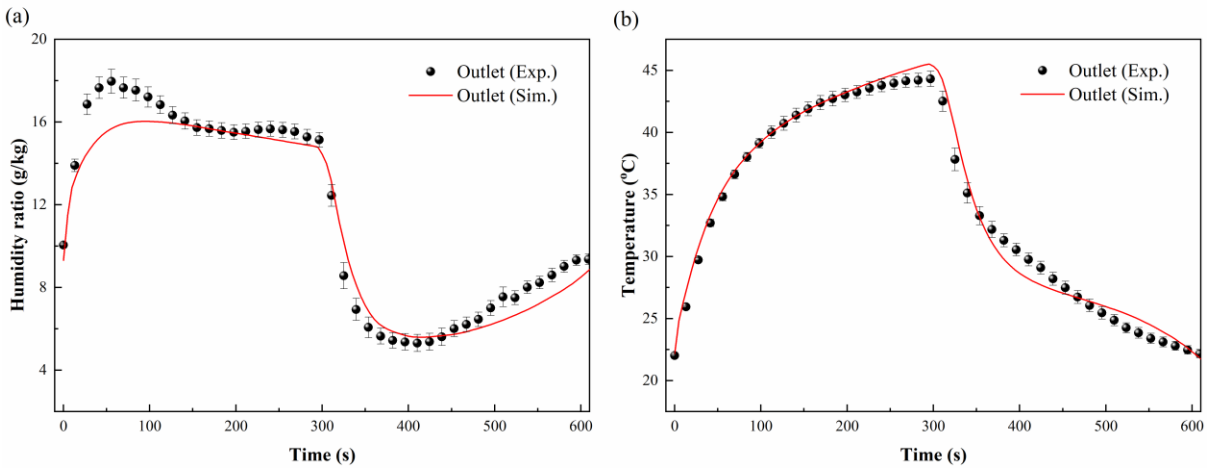

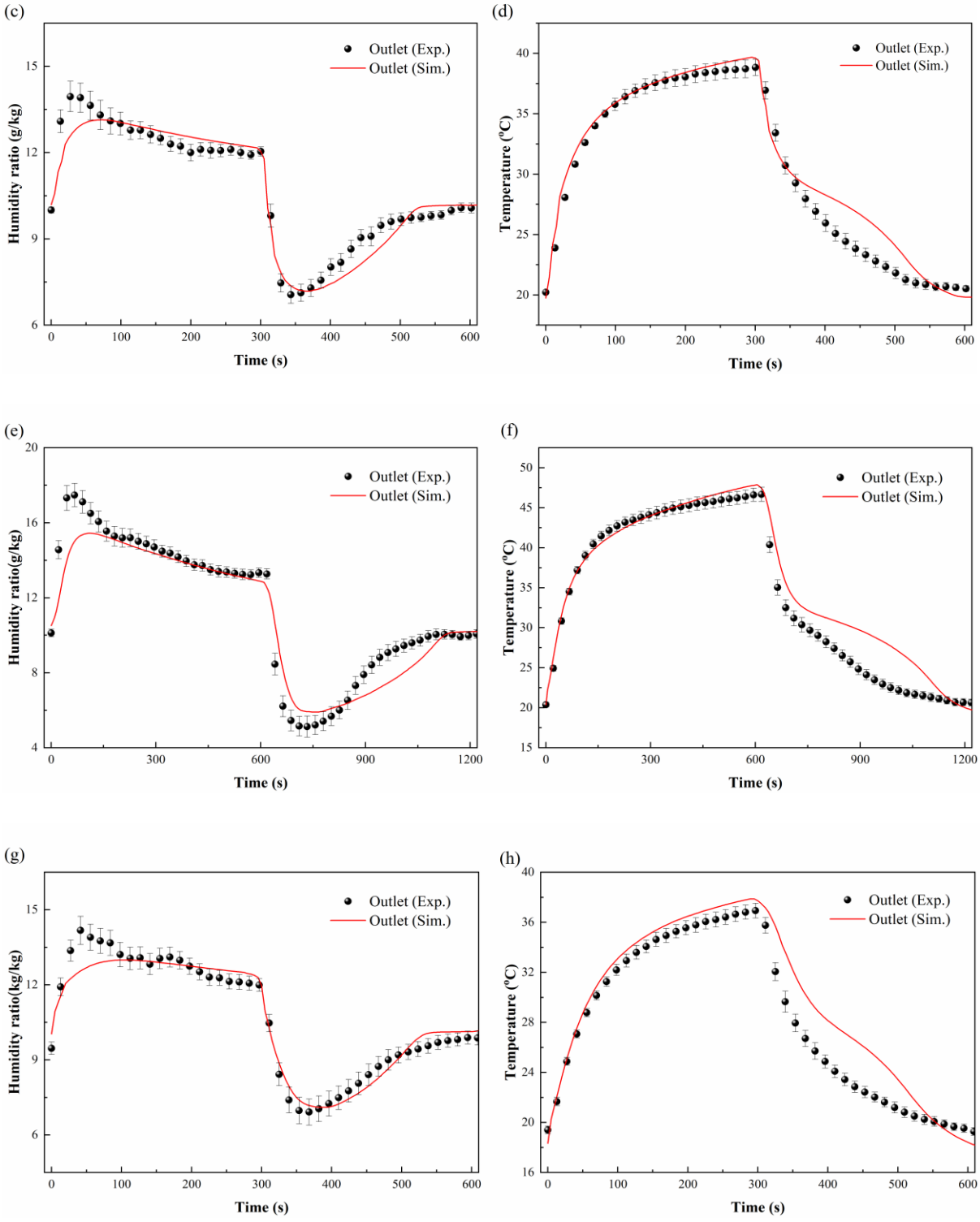

Fig. 5 Validation of the outlet air state in the computational model. (a-b) **Case 1**; (b-c) **Case 2**; (e-f) **Case 3**; and (g-h) **Case 4**.

Table 3

Operating parameters of different experimental cases.

	Mass flow rate (kg/h)	Equivalent heat flux (W/cm^2)	Cycle time (min)
Case 1	8.17	-0.6(AD)/2.4(De)	5
Case 2	16.35	-0.3(AD)/2.7(De)	5
Case 3	8.17	-0.15(AD)/2.4(De)	10
Case 4	8.17	-0.34(AD)/1.3(De)	5

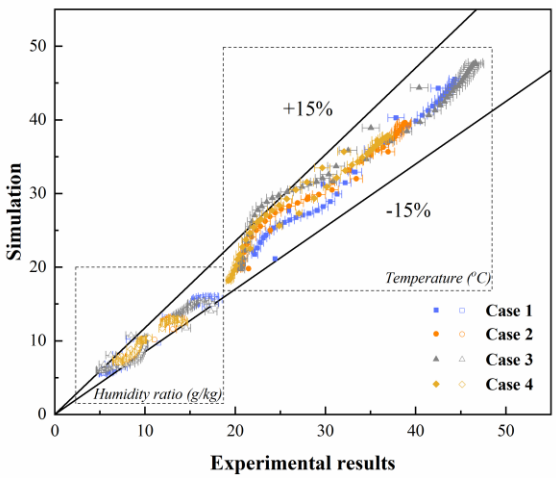

Fig. 6 Overall discrepancy between simulation and experiments.

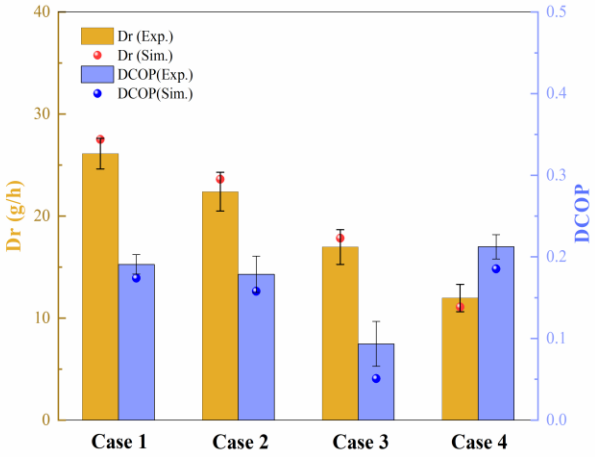

Fig. 7 Comparison of D_r and DCOP between experiments and simulation.

To further compare the operating performance of MOF-HP, D_r and DCOP of experimental and simulated results under different operation conditions (**Case 1, Case 2, Case 3 and Case 4**) are evaluated using Eqs. (31)-(33). From Fig. 7, it can be seen that the simulated D_r and DCOP are generally in agreement with the measured data. Thus, this computational modeling is able to predict the outlet air states of MOF-HP in a specific range. The measured results indicated that D_r and DCOP of **Case 1** generally outperform that of the other cases.

5. Parametric studies

The proposed modeling of heat and mass transfer has been judiciously validated through experiments in MOF-HP for the complete cycle. Here parametric studies are conducted to comprehensively investigate the effect of geometrical factors and flow field on the MOF-HP's performance. The operation parameters at the following simulations are referred to **Case 1,** as shown in Table 3.

5.1 $\overline{D_r}$ and DCOP

The performance of MOF-HP is investigated by varying the geometrical size of the unit channel. The horizontal length (L_x) of the heat sink has been increased from 5cm to 14cm, while the height (H_f) and width (W_y) of the unit channel have been changed from 2.5cm to 6cm and1mm to 3.5mm, respectively. These given sizes (L_x, H_f and W_y) defined the exterior framework of a unit channel inside the MOF-HP. The thickness of fin (W_f) and desiccant coating (W_d) are increased from 0.15mm to 0.55mm and 0.15mm to 0.6mm. All the unit channels have been simulated and analyzed with the same inlet air conditions. As for one complete operation cycle, the inlet air is dried during the dehumidification process and humidified during the regeneration process, which is controlled through the switchover of the bottom heat source.

Fig. 8 shows the variation of $\overline{D_r}$ and DCOP in one unit channel when changing the size (L_x, H_f, W_y, W_f, and W_d) of the flow passage. Fig. 8(a) indicates that $\overline{D_r}$ keeps increasing as L_x increases due to the extension of the unit channel (adding more desiccant coating), while DCOP has an evident increase only when $\gamma_l \geqslant 0.8$. In general, it is preferable to choose a longer L_x for the MOF-HP if there is a size limitation. In Fig. 8(b), it can be found that as the height of the fin

increases, there is the maximum $\overline{D_r}$ and DCOP with γ_f=0.7, and this indicates the trade-off between the heat transfer and mass transport. Similar to that case in Fig. 8(a), the variation of H_f can reflect the total amount of the desiccant coated in the channel and the total surface area of the coating layers. In this regard, though the higher H_f may facilitate the mass transport between the humid air and desiccant coatings, the increased heat resistance may reversely degrade the full adsorption capacity of the coatings. Subsequently, given the same inlet air velocity (~1.1m/s), Fig. 8(c) suggests that the wider size of the unit channel can result in more inlet air (mass flow rate) delivered into the MOF-HP, and then the increased $\overline{D_r}$ and DCOP are found, which means that the increase in the γ_y can improve the dehumidification of per unit channel. In addition, the thickness of the fin and desiccant coating can directly affect the heat and mass transfer of the unit channel. Fig. 8(d) presents the effect of W_f on the performance of MOF-HP. It is known that the increase in the thickness of the fin can decrease the thermal resistance of the whole heat sink but reversely increase the thermal capacitor ($m_{sink} \cdot c_{sink}$). With 0.3-1.1 of γ_f, $\overline{D_r}$ shows a slight decline from 1.47 g/h/per channel to 1.23 g/h/per channel, and DCOP is decreased from 0.25 to 0.16. As for the thickness of the desiccant coating, W_d, Fig. 8(e) shows that a thicker desiccant coating may improve the $\overline{Dr}$ to a certain degree, but as the thickness increases, $\overline{D_r}$ is decreased. DCOP shows a fast decrease and then maintained around 0.18. According to the results mentioned above, the best unit channel size group (10cm (l_x), 5cm (h_f), 4mm (W_y), 0.05mm (W_f), and 0.05mm (W_d)) is calculated and shown with 1.99 g/h/per channel and 0.29 of $\overline{D_r}$ and DCOP in Fig. 8(f), which is 1.59 and 1.51 times higher than that of the original **Case 1** (γ_l=γ_h=γ_y=γ_f=γ_d=1).

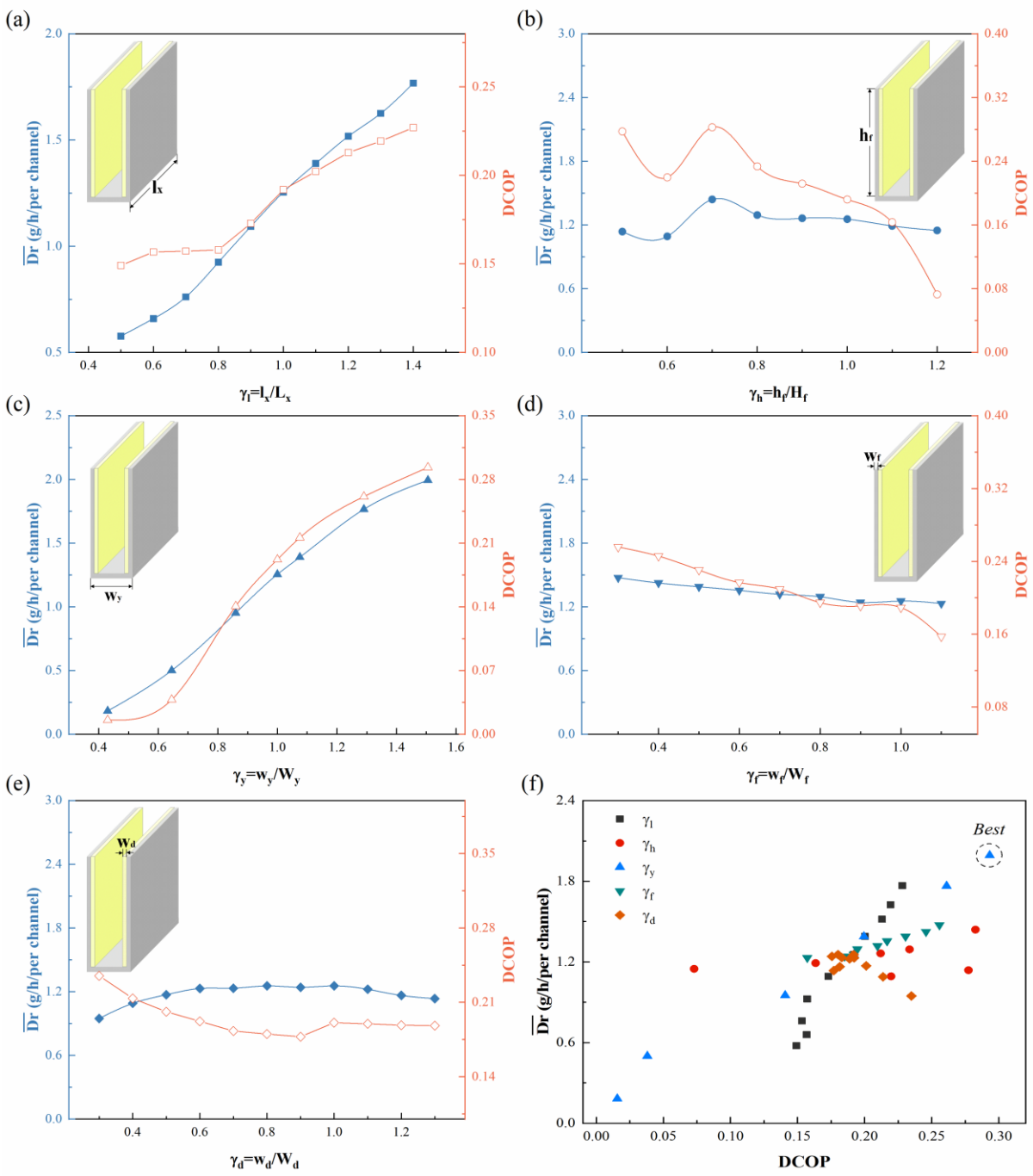

Fig. 8 Effect of geometric sizes on $\overline{D_r}$ and DCOP.

It should be noted that change of the inlet air velocity can also contribute to the fluctuation of the flow domain, which will affect the fluid flow and heat transfer (convective heat transfer). In Fig. 9, the effect of airflow rate ($\dot{m}_a$) on the dehumidification process has been investigated, which indicates that a low mass flow rate can have a relatively high DCOP but $\overline{D_r}$ is at a low

level, and as the mass flow rate increases, both $\overline{D_r}$ and DCOP reach the equilibrium state. Thus, by analyzing Eqs. (32) and (34), the increase in $\dot{m}_a$ will lead to the decrease of d_{in} - d_{out} and h_{in} – h_{out}, which means that the outlet air state is close to the inlet air state. If considering the supply power from the fan, the increased airflow rate may bring in a slight improvement in the dehumidification performance but consume more input energy.

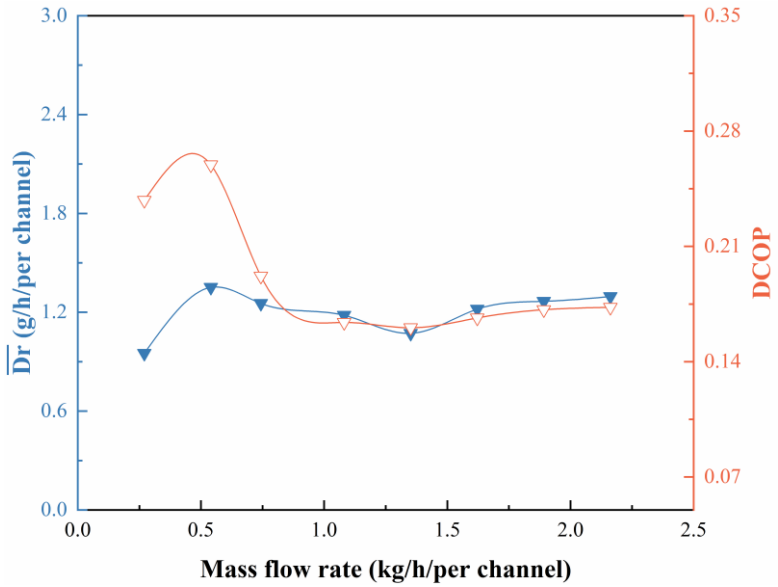

Fig. 9 Effect of mass flow rate on $\overline{D_r}$ and DCOP.

5.2 Reynolds number (*Re*), average Nusselt number ($Nu_{m,avg}$) and average thermal resistance ($R_{t,avg}$)

It is noted that the variation in the geometry of the unit channel of MOF-HP can vary the flow state of the incoming fluid and the inside heat transfer. And the heat transfer inside the unit channel can directly affect the dehumidification and regeneration of the desiccant coating. For example, an ultralow flow state may deteriorate the dehumidification performance because of the extra heat accumulation. In contrast, an ultrafast flow state can reduce the regeneration capacity due to the strengthened heat transfer. In this regard, it is essential to explore the

relationship between the geometry of the designed channel and the flow and heat transfer field, as shown in Fig. 10.

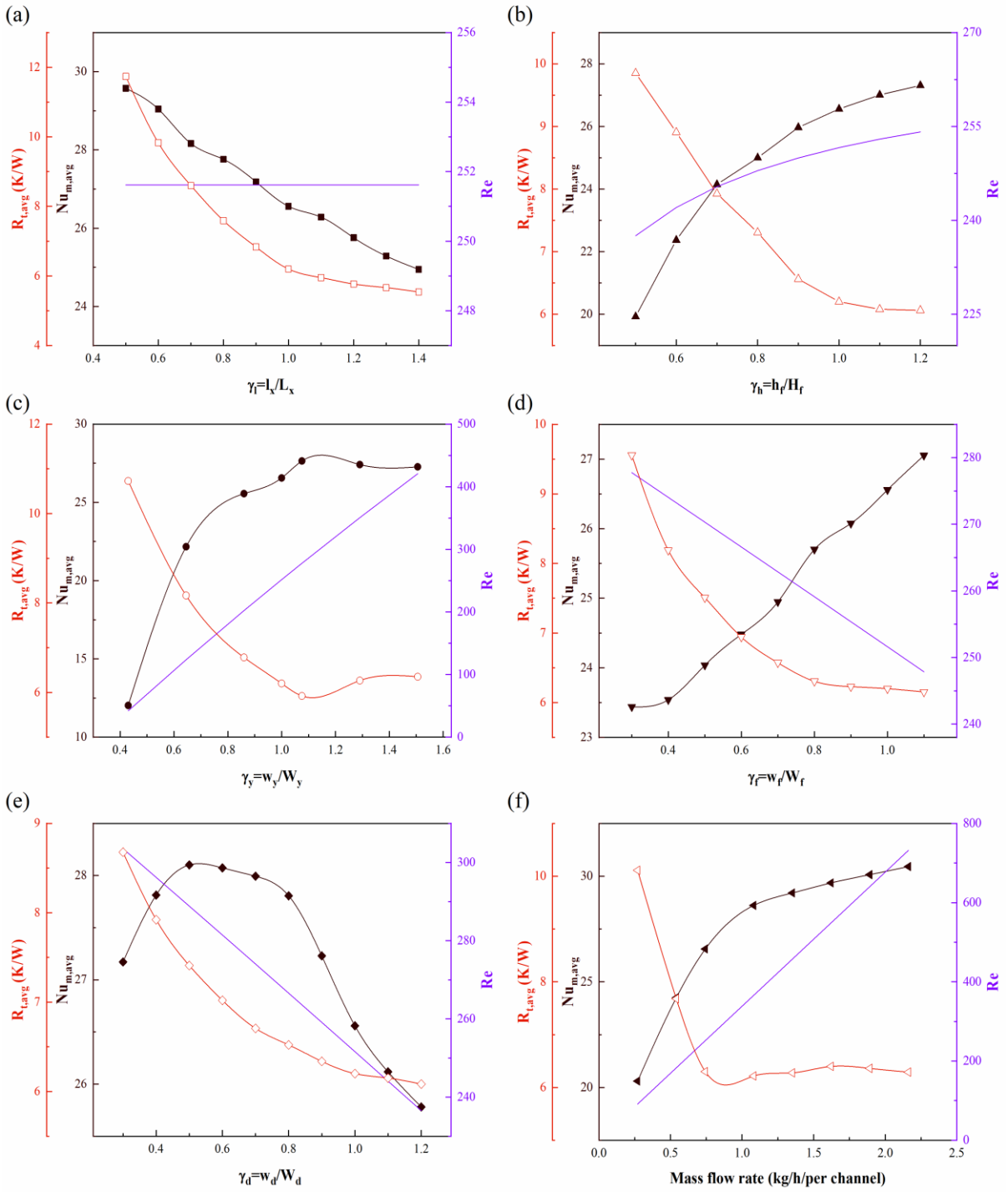

Fig. 10 Effect of geometric sizes and mass flow rate on Re and R_t.

Fig. 10(a) shows that the extension (γ_l) of the channel cannot change the flow state (*Re*) but both $Nu_{m,avg}$ and $R_{t,avg}$ experience a downward trend. According to Eqs. (36-37), the average bottom temperature increases as the γ_l increases, and $R_{t,avg}$ maintained around 6K/W with $\gamma_l \geqslant 1$. In addition, the change of other geometrical sizes (γ_h, γ_y, γ_f and γ_d) can all affect the characteristic length, and thus the flow state (Re) and heat transfer ($Nu_{m,avg}$). The higher fin of the unit channel can result in an increased amount of incoming air. In Fig. 10(b), it can be found that $Nu_{m,avg}$ has been improved, and the average thermal resistance is reduced. The general trend of both $Nu_{m,avg}$ and $R_{t,avg}$ approaches a specific range if $\gamma_h \geqslant 1$. When increasing the width of the unit channel (W_y), there is the optimum value for the heat transfer located at γ_y of 1.07 due to the maximum $Nu_{m,avg}$ and the minimum $R_{t,avg}$. Similar to the case by varying H_f, both $Nu_{m,avg}$ and $R_{t,avg}$ are finally reaching a specific range when $\gamma_y \geqslant$ 0.86. In Fig. 10(d), the increased thickness of the fin can facilitate the heat transfer though there is a slight decrease in the Reynolds number (Re). Considering that metallic fins have high thermal conductivity (low thermal resistance), the larger γ_f is, the less the whole thermal resistance can be found. Fig. 10(e) indicates the variation of $Nu_{m,avg}$ and $R_{t,avg}$ with different coating thicknesses. As expressed by Eq. (38), the downward trend of $R_{t,avg}$ implies that the maximum temperature at the bottom side of the heat sink decreases as γ_d increases. The change of $Nu_{m,avg}$ indicates that the optimum value of γ_d for the heat transfer is between 0.4-0.8 of γ_d. Except for the effect of the geometrical size on the fluid flow and heat transfer, the varied mass flow rate has been investigated, as shown in Fig. 10(f). it can be seen that the $R_{t,avg}$ drops sharply to ~6K/W when the mass flow rate per channel is larger than 0.75kg/h. Besides, the flow state and the heat transfer gain a specific increase with the increased mass flow rate. Integrating with the dehumidification performance calculated in Fig. 10, the mass flow rate may slightly improve the whole operation performance if using the same heat flux from the

bottom surface. To further improve the dehumidification performance, the operation conditions with a high mass flow rate are supposed to match a higher temperature heat source (improvement of regeneration conditions).

5.3 η_1 and η_2

To better understand the effect of using desiccant coating on the surface of the fin, an analysis has been conducted on the varied thickness of the desiccant coating for a unit channel inside MOF-HP. The objective of this analysis aims to assess the heat transfer and the air conditions of the outlet air under different thickness of desiccant coatings. In this regard, heat transfer effectiveness (η_1) and sensitivity coefficient (η_2) have been defined to compare with the reference group. From Fig. 11, it is indicated that the increase of coating thickness can improve limited heat transfer effectiveness if W_d>0.35mm, which means that the average bottom temperature can be maintained at a certain level under the same inlet air conditions and bottom heat flux. In addition, the sensitivity coefficient (η_2) shows the relationship of the removed latent load (represented by the dehumidification capacity) to the variation of the whole air load (sensible and latent loads). Thus, the calculated results in Fig. 11 demonstrated that the optimal coating thickness is between 0.3-0.5mm, which can make use of its ability to match the dehumidification capacity.

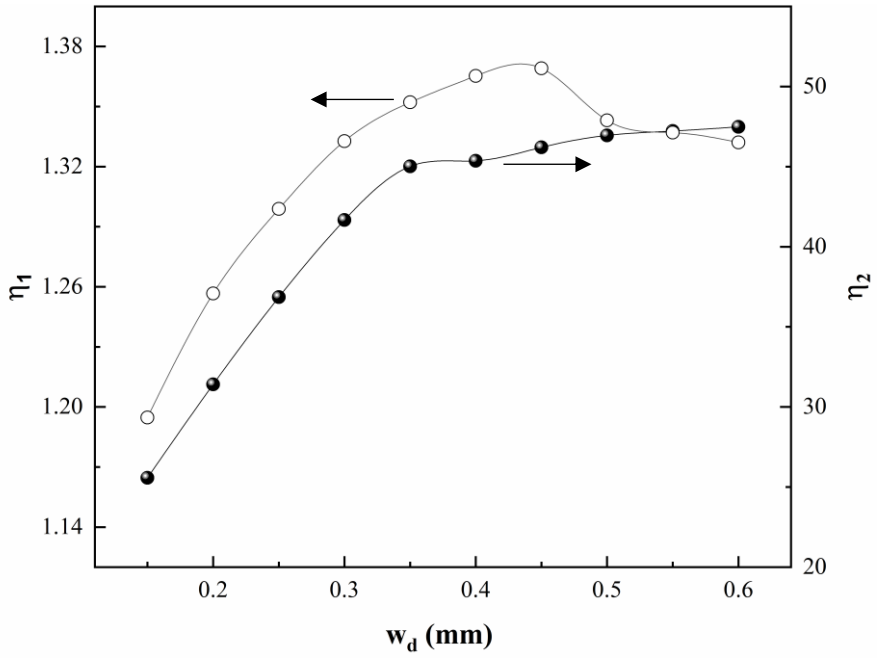

Fig. 11 Effect of desiccant coatings on η_1 and η_2.

6. Conclusion

In this work, the application of solid desiccant coatings on the unit channel of MOF-HP towards the thermal and moisture transport enhancement has been analyzed to provide the optimized geometrical design of the unit channel considering the fluid flow, heat transfer, and moisture transport. The conclusions can be shown as follows:

1) Compared with the conventional air conditioning system, the desiccant-coated humidity pump can regulate the latent load of the surrounding air above the dew point, avoiding the overcooling process.

2) The increase in length (L_x) and width (W_y) of the unit channel can remarkably improve its dehumidification capacity, while the other three sizes (H_f, W_f, and W_d) have a limited effect on the dehumidification capacity. According to the geometry optimization, the best size among the calculated results shows 1.99 g/h/per channel and 0.29 of $\overline{\mathrm{Dr}}$ and DCOP, 1.59 and 1.51 times higher than that of **Case 1**.

3) The increase in the mass flow rate can affect the dehumidification process at the low mass flow rate range. After a specific value, both $\overline{D_r}$ and DCOP maintained at the constant level.

4) Based on the comprehensive analysis on the flow field and heat transfer, the increase in the sizes (L_x, H_f, W_y, W_f, and W_d) and mass flow rate all can reduce the average thermal resistance, but only the increase in the H_f, W_f, and mass flow rate can lead to the increase in the average Nusselt number. Besides, the thickness of desiccant coatings between 0.5-0.8 of γ_d may show the best thermodynamic performance.

5) Compared with the bare heat sink, the utilization of desiccant coatings can increase the average surface heat transfer coefficient (related to average bottom temperature) to a certain degree and then be maintained at a constant level. The sensitivity coefficient shows that the desiccant coating can improve the latent load handling, and the recommended thickness of the desiccant is between 0.3-0.5mm.

Since the geometry of the flow channel of a MOF-HP can affect the flow state and thus the heat and mass transfer, the above computational analysis can provide some guidelines to design the optimized geometry of each unit flow channel. Besides, the selection of the desiccant and the integration with different heat sources are also crucial for the full-scale design of the compact solid desiccant humidity pump.

Acknowledgements

The authors acknowledge the financial support from the Chinese Scholarship Council (No. 201806230288) and the Bjarne Saxhof's Foundation.

Nomenclature

c	Concentration, mol/m^3	ρ	Density, kg/m^3
C_p	Specific heat capacity, J/kg K	μ	Dynamic viscosity, Pa/S
D	Mass diffusivity, m^2/s	λ	Thermal conductivity, W/(m·K)
$DCOP$	Dehumidification coefficient of performance	φ	Relative humidity
$\vec{g}, \vec{J}$	Concentration gradient, mol/(m· s)	η	Ratio
k	Ad/desorption rate, 1/s	Ω	The net heat change between the inlet and outlet air, J
L, W, H	Length, width and height of the unit channel, m	*Subscripts*	
$\dot{m}$	Mass flow rate, kg/s	a	Air
M	Molecular mass, mol/kg	Al	Aluminum
NUM	Number of fins	d	Desiccant
p	Pressure, Pa	eq	Equilibrium
$\vec{q}$	Heat flux vector, W/m^2	s	Heat sink
q_m	Mass flux, mol/(m^2 ·s)	S	Surface
q_h	Heat flux, W/m^2	v	Vapor
R	Gas constant, J/ mol K	w	Water
R_t	Thermal resistance, K/W	*Non-dimensional number*	
T	Temperature, K	Nu	Nusselt number
t	Time, s	Re	Reynolds number
$\vec{u}$	Velocity vector, m/s		

$\bar{W}$	The amount of the adsorbed vapor, kg/kg

References

[1] International Energy Agency, "The Future of Cooling," www.iea.org/reports/the-future-of-cooling. 2018.

[2] Rupp, R.F., Vásquez, N.G., Lamberts, R. A review of human thermal comfort in the built environment. *Energy and Buildings*, 2015. 105: 178-205.

[3] Renalds, A., Smith T.H., Hale P.J., A systematic review of built environment and health. *Family & Community Health*, 2010. **33**(1).

[4] Luo, X., Chang, B., Tian, W., Li, J., Gu, Z. Experimental study on local environmental control for historical site in archaeological museum by evaporative cooling system. *Renewable Energy*, 2019. **143**: 798-809.

[5] Chua, K.J., Chou, S.K., Yang, W.M., Yan, J. Achieving better energy-efficient air conditioning – A review of technologies and strategies. *Applied Energy*, 2013. **104**: 87-104.

[6] Zu, K., Qin M.H., Cui, S. Progress and potential of metal-organic frameworks (MOFs) as novel desiccants for built environment control: A review. *Renewable and Sustainable Energy Reviews*, 2020. **133**: 110246.

[7] Song, W.F., Zhang, Z.R., Chen, Z.H., Wang, F.M., Yang, B. Thermal comfort and energy performance of personal comfort systems (PCS): A systematic review andmeta-analysis. *Energy and Buildings*, 2022. **256**: 111747.

[8] Zhao, L.H., Wang, R.Z., Ge, T.S. Desiccant coated heat exchanger and its applications. *International Journal of Refrigeration*, 2021. **130**: 217-232.

[9] Qin M., Hou P., Wu Z., and Wang J. Precise humidity control materials for autonomous regulation of indoor moisture, *Building and Environment*, 2020. **169**: 106581.

[10] Ge, T.S., Dai, Y.J., Wang, R.Z. Review on solar powered rotary desiccant wheel cooling system. *Renewable and Sustainable Energy Reviews*, 2014. **39**: 476-497.

[11] Jani, D.B., Mishra M., Sahoo P.K., Solid desiccant air conditioning – A state of the art review. *Renewable and Sustainable Energy Reviews*, 2016. **60**: 1451-1469.

[12] Han, X., Zhang, X., Wang, L., Niu, R. A novel system of the isothermal dehumidification in a room air-conditioner. *Energy and Buildings*, 2013. **57**: 14-19.

[13] La, D., Li, Y., Dai, Y.J., Ge, T.S., Wang, R.Z. Development of a novel rotary desiccant cooling cycle with isothermal dehumidification and regenerative evaporative cooling using thermodynamic analysis method. *Energy*, 2012. **44**(1): 778-791.

[14] Tu, Y.D., Wang, R.Z., Ge, T.S., Zheng, X. Comfortable, high-efficiency heat pump with desiccant-coated, water-sorbing heat exchangers. *Scientific Reports*, 2017. **7**(1): 40437.

[15] Ge, T.S., Dai, Y.J., Li, Y., Wang, R.Z. Simulation investigation on solar powered desiccant coated heat exchanger cooling system. *Applied Energy*, 2012. **93**: 532-540.

[16] Ge, T.S., Dai, Y.J., Wang, R.Z., Peng, Z.Z. Experimental comparison and analysis on silica gel and polymer coated fin-tube heat exchangers. *Energy*, 2010. **35**(7): 2893-2900.

[17] Jiang, Y., Ge, T.S., Wang, R.Z., Hu, L.M. Experimental investigation and analysis of composite silica-gel coated fin-tube heat exchangers. *International Journal of Refrigeration*, 2015. **51**: 169-179.

[18] Vivekh, P., Bui, D.T., Kumja, M., Islam, M.R., Chua, K.J. Theoretical performance analysis of silica gel and composite polymer desiccant coated heat exchangers based on a CFD approach. *Energy Conversion and Management*, 2019. **187**: 423-446.

[19] Fathieh, F., Dehabadi, L., Wilson, L.D., Besant, R.W., Evitts, R.W. Sorption study of a starch biopolymer as an alternative desiccant for energy wheels. *ACS Sustainable Chemistry & Engineering*, 2016. **4**(3): 1262-1273.

[20] Dehabadi, L., Fathieh, F., Wilson, L.D., Evitts, R.W., Simonson, C.J. Study of dehumidification and regeneration in a starch coated energy wheel. *ACS Sustainable Chemistry & Engineering*, 2017. **5**(1): 221-231.

[21] Li, B., Hua, L., Tu, Y., Wang, R.Z. A full-solid-state humidity pump for localized humidity control. *Joule*, 2019. **3**(6): 1427-1436.

[22] Cui, S., Qin, M.H., Marandi, A., Steggles, V., Wang, S., *et al*. Metal-organic frameworks as advanced moisture sorbents for energy-efficient high temperature cooling. *Scientific Reports*, 2018. **8**(1): 15284.

[23] Kummer, H., Jeremias, F., Warlo, A., Füldner, G., Fröhlich, D., *et al*. A Functional full-scale heat exchanger coated with aluminum fumarate metal–organic framework for adsorption heat transformation. *Industrial & Engineering Chemistry Research*, 2017. **56**(29): 8393-8398.

[24] Hou, P., Qin, M., Cui, S., Zu, K. Preparation and characterization of metal-organic framework /microencapsulated phase change material composites for indoor hygrothermal control. *Journal of Building Engineering*, 2020. **31**: 101345.

[25] Canivet, J., Fateeva, A., Guo, Y.M., Coasne, B., Farrusseng, D. Water adsorption in MOFs: fundamentals and applications. *Chemical Society Reviews*, 2014. **43**(16): 5594-5617.

[26] Henninger, S.K., et al., MOFs for Use in adsorption heat pump processes. European *Journal of Inorganic Chemistry*, 2012. **2012**(16): 2625-2634.

[27] Cadiau, A., Lee, J.S., Borges, D.D., Fabry, P., Devic, T., et al. Design of hydrophilic metal organic framework water adsorbents for heat reallocation. *Advanced Materials*, 2015. 27: 4775-4780.

[28] Permyakova, A., Skrylnyk, O., Courbon, E., Affram, M., Wang, S.J., *et al*. Synthesis optimization, shaping, and heat reallocation evaluation of the hydrophilic metal–organic framework MIL-160(Al). *ChemSusChem*, 2017. **10**(7): 1419-1426.

[29] Schlüsener, C., Xhinovci, M., Ernst, S.J., Schmitz, A., Tannert, N., *et al*. Solid-solution mixed-linker synthesis of isoreticular Al-based MOFs for an easy hydrophilicity tuning in water-sorption heat transformations. *Chemistry of Materials*, 2019. **31**(11): 4051-4062.

[30] Hou, P., Zu, K., Qin, M.H., Cui, S. A novel metal-organic frameworks based humidity pump for indoor moisture control. *Building and Environment*, 2021. **187**: 107396.

[31] Cui, S., Marandi, A., Lebourleux, G., Thimon, M., Bourdon, M. Heat properties of a hydrophilic carboxylate-based MOF for water adsorption applications. *Applied Thermal Engineering*, 2019. **161**: 114135.

[32] Li, Z., Michiyuki, S., Takeshi, F., Experimental study on heat and mass transfer characteristics for a desiccant-coated fin-tube heat exchanger. *International Journal of Heat and Mass Transfer*, 2015. **89**: 641-651.

[33] Jagirdar, M., Lee, P.S. Mathematical modeling and performance evaluation of a desiccant coated fin-tube heat exchanger. *Applied Energy*, 2018. **212**: 401-415.

[34] Ghahremannezhad, A., Vafai, K. Thermal and hydraulic performance enhancement of microchannel heat sinks utilizing porous substrates. *International Journal of Heat and Mass Transfer*, 2018. **122**: 1313-1326.

[35] Ali, M., Vukovic, V., Sahir, M.H., Basciotti, D. Development and validation of a desiccant wheel model calibrated under transient operating conditions. *Applied Thermal Engineering*, 2013. **61**(2): 469-480.

[36] Flossmann, A.I., Hall, W.D., Pruppacher, H.R. A theoretical study of the wet removal of atmospheric pollutants. Part I: The redistribution of aerosol particles captured through nucleation and impaction scavenging by growing cloud drops. *Journal of the Atmospheric Sciences*, 1985. **42**(6): 583-606.

[37] Zu, K., Qin, M.H. Experimental and modeling investigation of water adsorption of hydrophilic carboxylate-based MOF for indoor moisture control. *Energy*, 2021. **228**: 120654.

[38] Sircar, S., Hufton, J.R. Why Does the linear driving force model for adsorption kinetics work? *Adsorption*, 2000. **6**(2): 137-147.

[39] Zu, K., Qin, M., Rode, C., Libralato, M. Development of a moisture buffer value model (MBM) for indoor moisture prediction. *Applied Thermal Engineering*, 2020. **171**: 115096.